Journal of Advanced Ceramics
2024, **13**(11): 1795–1806
https://doi.org/10.26599/JAC.2024.9220977

Research Article

Etching-time-regulated strategy toward delaminated Mo_2CT_x MXene for tailoring electromagnetic wave absorption

Yukai Chang[1,2], Huilan Zhao[1], Xin Liu[2], Yingjie Huo[3,✉], Binbin Dong[4], Libo Wang[1], Hari Bala[1], Qianku Hu[1], Aiguo Zhou[1,✉]

[1] *School of Materials Science and Engineering, Henan Polytechnic University, Henan 454003, China*
[2] *Key Laboratory of Dielectric and Electrolyte Functional Material Hebei Province, Northeastern University at Qinhuangdao, Qinhuangdao 066004, China*
[3] *School of Physical Science and Technology, Tangshan Normal University, Tangshan 063000, China*
[4] *School of Material Science and Engineering, Luoyang Institute of Science and Technology, Luoyang 471023, China*

Received: July 29, 2024; Revised: September 7, 2024; Accepted: September 23, 2024

Abstract: MXene-based absorbers have shown promising application prospects because of their sophisticated structural design and clever material composites. However, the intrinsic MXene materials themselves have not achieved significant breakthroughs in microwave absorption (MA) performance. Therefore, the development of novel and efficient pure MXene absorbing materials is imperative to address inherent mismatches in electromagnetic parameters, highlighting the urgent need in this area. Here, a straightforward strategy involving etching time modulation is proposed to customize the electromagnetic wave (EMW) absorption properties of delaminated Mo_2CT_x MXene. The impact of varying etching degrees on the EMW absorption capabilities of Mo_2CT_x MXenes was systematically investigated through controlled etching durations of Mo_2Ga_2C MAX phase. Among them, the sample etched for 12 h achieved an effective absorption bandwidth (EAB) of 4.4 GHz at an ultrathin thickness of 1.3 mm, and the strongest reflection loss (RL) value was as high as −60.7 dB when the sample etching time was increased to 24 h. The improvement in absorbing performance was attributed to the dielectric loss and polarization process induced by terminal functional groups and surface-rich defects, which optimized impedance matching. This work establishes that intrinsic Mo_2CT_x MXene materials with superior absorbing properties outperform traditional pure MXenes, providing a strong basis for advancing Mo-based MXene absorptive materials.

Keywords: MXene; Mo_2CT_x; microwave absorption (MA); defect engineering; polarization process

1 Introduction

With the wide application of electromagnetic waves (EMWs) in people's lives, the issue of EMW pollution has escalated, significantly impacting both daily life and health [1]. EMW-absorbing materials are capable of converting incident EMW energy into other forms of consumption, thereby effectively mitigating EMW pollution. These materials find utility in the design and manufacture of radar stealth or electromagnetic defense materials, which safeguard electronic equipment, buildings, warplanes, and even the human body from the adverse effects of electromagnetic radiation [2]. Hence, the development of EMW-absorbing materials with wide frequency coverage, minimal thickness, lightweight construction, and robust absorption capabilities holds paramount importance in curtailing EMW pollution [3,4]. In recent years, researchers have identified various efficient EMW-absorbing materials, among which two-dimensional (2D) materials have emerged as highly competitive and promising candidates because of their exceptional EMW attenuation properties. MXenes stand as a quintessential exemplar within this category [5,6].

MXenes are a collective group comprising 2D transition metal carbides, nitrides, and carbon nitrides [7]. The general formula is $M_{n+1}X_nT_x$, where M stands for early transition metals (such as Ti, Mo, and Nb), X usually represents carbon and/or nitrogen, $n = 1$, 2, or 3, and T_x denotes surface terminations (=O, –OH, and/or –F). As the most widely studied 2D materials, it is typically obtained by selectively removing the "A-element" layer in MAX phase, a ternary compound characterized by a layered structure, where A represents a group A element (Al, Ga, etc.) [8–10]. The distinctive characteristics of MXenes, such as excellent conductivity and a surface rich in functional groups, have garnered considerable interest in various applications, including hydrogen storage [11], hydrolysis catalysis [12], energy storage [13], and particularly microwave absorption (MA). Currently, MXene-based absorbers are predominantly centered around $Ti_3C_2T_x$ and its composites. Cui *et al.* [14] achieved a reflection loss (RL) value of −40.8 dB at a thickness of 1.45 mm by optimizing key parameters in the etching process of $Ti_3C_2T_x$ MXene. However, the effective absorption bandwidth (EAB) was only 3.66 GHz at 1.68 mm. Du *et al.* [15] further improved MA performance by adjusting the surface functional groups and interlayer spacing of $Ti_3C_2T_x$ MXene, and their RL and EAB increased to −49.1 dB and 3.9 GHz, respectively. However, pure $Ti_3C_2T_x$ MXene typically exhibits insufficient dielectric loss characteristics because of their high electrical conductivity, leading

---

✉ Corresponding authors.
E-mail: Y. Huo, 127081@tstc.edu.cn;
A. Zhou, zhouag@hpu.edu.cn

清華大学出版社 Tsinghua University Press | SciOpen

to unimpressive electromagnetic absorption performance. Many researchers have focused on the design of $Ti_3C_2T_x$-based composite absorber materials in recent years, resulting in numerous research achievements in this field. For example, $Ti_3C_2T_x$ MXene has been combined with magnetic materials (such as Co, Ni, and FeCo) [16–18], carbon-based materials (graphene, carbon nanotubes, and carbon nanoparticles) [19,20], and dielectric materials (MoS_2, polypyrrole, and SiC) [21–23]. Although $Ti_3C_2T_x$-based composite materials have shown improved absorption performance compared with that of pure $Ti_3C_2T_x$ MXene to some extent, it is difficult to meet practical application requirements because of the complex sample preparation process. Some researchers have also explored other types of MXene-based absorbing materials, such as $V_{n+1}C_nT_x$ MXenes (V_2CT_x and $V_4C_3T_x$) [24], Ti_2CT_x nanosheets [25], and Nb_2CT_x/Nb_2O_5 composites [26]. Although these non-$Ti_3C_2T_x$-based MXenes demonstrate some absorption capabilities, they do not fulfill the criterion of being the "lightweight, thin, broadband, and strong" required for high-performance microwave absorbing materials. In view of the current research status of MXene-based absorbing materials, the development of new type of pure MXene materials to meet the needs of high-performance absorbing materials without cumbersome composite material preparation processes is urgently needed.

Mo_2CT_x MXene is an important type of MXenes with excellent specific surface areas (SSAs) and tunable surface chemistry characteristics. Relevant calculations show that Mo presents higher activity and stability than other transition metals, such as Ti and V [27,28]. Some researchers have introduced Mo atoms into 312-type MAX phase in an orderly manner to construct a new type of $Mo_2TiC_2T_x$ MXene by selective etching, which results in excellent EMW absorption performance [29]. Additionally, β-phase molybdenum carbide is usually combined with carbon materials to achieve efficient EMW absorption performance because of its good dielectric properties and structural controllability [30]. On the basis of these findings, Mo_2CT_x MXene with 2D structure derived from 221-type MAX phase Mo_2Ga_2C may holds promising applications in the field of EMW absorption, but unfortunately, it has not been studied in this field until now. Currently, the literature on Mo_2CT_x MXene have focused primarily on catalysis, thermoelectric properties, and electrochemistry, with limited coverage of the systematic investigation of the wave-absorbing characteristics of Mo_2CT_x MXene. Therefore, investigating the microwave-absorbing properties of Mo_2CT_x MXene is crucial.

Herein, a series of Mo_2CT_x samples with different etching degrees were customized via a facile hydrothermal etching method by precisely controlling different etching time, and the sample quality and MA performance of the Mo_2CT_x nanosheets were modulated. Poor absorption performance is observed in the intrinsic Mo_2Ga_2C MAX phase owing to mismatched electromagnetic parameters, but its microwave-absorbing properties are greatly improved with etching due to improved impedance matching and polarization loss. The sample of delaminated Mo_2CT_x etched for 12 h from Mo_2Ga_2C MAX phase achieved a maximum EAB of 4.4 GHz at an ultrathin thickness of 1.3 mm. As the etching time increased, the conductivity decreased; thus, the loss of conductivity decreased. However, the presence of hydrochloric acid (HCl) leads to an increase in surface defects, triggering more polarization processes and finally achieving a good impedance matching balance. The strongest RL value is as high as −60.7 dB when the sample etching time is increased to 24 h. As of now, Mo_2CT_x has exhibited the strongest electromagnetic absorption performance among all pure MXenes, showing promise as a focal point for research on next-generation MXene-based absorbing materials.

2 Experimental

2.1 Materials

The materials utilized in the experiment included molybdenum powder (Mo, 99.5 wt%, metals basis, 2 μm, Macklin, China), carbon powder (C, 3 μm, Beijing Xingrongyuan Co., Ltd., China), gallium pellets (Ga, 99.99 wt%, Beijing Xingrongyuan Co., Ltd., China), ammonium fluoride (NH_4F, 98.0 wt%, Aladdin, China), and HCl (11.8 mol/L, Shuangshuang Chemical, China). All reagents were commercially purchased at analytical grade and were used without further purification.

2.2 Preparation of Mo_2Ga_2C (MAX)

The mixture of Mo powder and C powder at a certain molar ratio was placed into a tube furnace (GSL-1700X, Hefei Kejing Material Technology Co., Ltd., China), and then, the sample was heated at 1000 °C for 12 h with flow of Ar gas. After the reaction was completed and cooled to room temperature, β-Mo_2C was obtained, followed by sieving.

The resulting β-Mo_2C and Ga raw materials were mixed homogeneously at a molar ratio of 5 : 1 and vacuum-sealed in a quartz tube. The mixture was subsequently subjected to heat treatment at 650 °C for 16 h, resulting in the synthesis of Mo_2Ga_2C MAX phase precursor powder.

2.3 Preparation of Mo_2CT_x (MXene)

2 g of NH_4F was first adequately dissolved in 40 mL of 6 M HCl as an etching solution and then transferred to 100 mL of polytetrafluoroethylene liner. After that, 1 g of Mo_2Ga_2C powder was immersed in the above etching solution, mechanically stirred for approximately 20 min, and ultrasonic treatment was performed for 30 min to ensure that the solution was complete. Then, the liner was sealed with a hydrothermal stirrer, heated at 160 °C for 6, 12, 24, or 36 h for the etching process, and then allowed to cool to room temperature naturally. Afterwards, the obtained acidic product was washed repeatedly with deionized water (DI), centrifuged until pH reached 6, and then washed with ethanol three times. Finally, the product was collected after vacuum drying at 60 °C for 12 h. According to the etching time, the four samples obtained were denoted Mo_2CT_x-6H, Mo_2CT_x-12H, Mo_2CT_x-24H, and Mo_2CT_x-36H.

2.4 Characterizations

An X-ray diffractometer (XRD; Smart Lab, Rigaku, Japan) was carried out to analyze the structure and characterize the physical phase in the range of 5°–80°. A Raman spectroscope (Renishaw, UK) with a 532 nm laser was used to analyze the bonding state and chemical structure. A field emission scanning electron microscope (FE-SEM, Merlin Comp, Carl Zeiss NTS GmbH, Germany) was used to observe the microscopic morphology and energy dispersive spectroscopy (EDS) mapping scans. The particle size and crystal structure were observed via a transmission electron microscope (JEM-F200, JEOL, Japan) at an accelerating voltage of 200 kV. Chemical element analysis was performed via an X-ray photoelectron spectroscope (XPS, ESCALAB 250Xi, Thermo Scientific, USA). SSAs was characterized via a nitrogen adsorption–desorption test (ASAP 2020, Micromeritics Instrument Co., Ltd., USA) at 77 K.

2.5 Microwave test methods

The tested samples were prepared by homogeneously mixing the samples with paraffin wax at a sample-to-wax mass ratio of 80 : 20 and then pressing them into a dense ring-shaped body with an inner diameter (Φ_{in}) of 3.04 mm and an outer diameter (Φ_{out}) of 7.00 mm. A vector network analyzer (E5080B, Keysight Technologies, Inc., USA) was used to test the dielectric constant and permeability in the frequency range of 2.0–18.0 GHz and calculate RL values. RL value can be calculated according to Eqs. (1) and (2) [31]:

$$\mathrm{RL}\,(\mathrm{dB}) = 20\log_{10}\left|(Z_{\mathrm{in}} - Z_0)/(Z_{\mathrm{in}} + Z_0)\right| \tag{1}$$

$$Z_{\mathrm{in}} = Z_0\sqrt{\frac{\mu_{\mathrm{r}}}{\varepsilon_{\mathrm{r}}}}\tanh\left(\mathrm{j}\left(\frac{2\pi fd}{c}\right)\sqrt{\varepsilon_{\mathrm{r}}\mu_{\mathrm{r}}}\right) \tag{2}$$

where Z_{in} is the input characteristic impedance of absorber, Z_0 is the input impedance of free space, μ_{r} denotes the relative permeability, ε_{r} denotes the complex permittivity, f denotes the frequency, d denotes the thickness of the absorber, and c is 3.0×10^8 m/s (speed of light).

3 Results and discussion

3.1 Preparation process and characterization and structural analysis of Mo_2CT_x

The preparation route of Mo_2CT_x MXene with varying degrees of defects is illustrated in Fig. 1. The lamellar structure of Mo_2Ga_2C MAX phase was synthesized via a two-step sintering method in a tube furnace filled with Ar gas on the basis of our earlier research. Mo_2CT_x MXene nanosheets with widened interlayer spacing were obtained after the selective removal of Ga atom layers with an etching solution via a simple hydrothermal method. Moreover, surface defects and functional groups can be controlled by changing the etching time. XRD patterns of Mo_2Ga_2C MAX phase and Mo_2CT_x MXene with different etching time are displayed in Fig. 2(a). All intense characteristic peaks (100), (103), (008), and (005) of the raw precursor powder clearly match well with Mo_2Ga_2C MAX phase, indicating the successful preparation of Mo_2Ga_2C MAX phase [32]. After the etching process, the peak at 9.8° (002) for Mo_2Ga_2C disappears, whereas the peak at 8.7° increases, confirming the successful removal of Ga from MAX, which significantly enlarges the layer spacing of Mo_2CT_x. Moreover, the main diffraction peak (008) at approximately 40 °C for Mo_2Ga_2C diminished or disappeared, further validating the fabrication of high-quality Mo_2CT_x MXene [33]. The corresponding XRD patterns of (002) feature peak with a detailed range from 7° to 12° are enlarged in Fig. 2(b). Notably, the peak at 9.85° is weakened, and a peak at 8.67° appears in the Mo_2CT_x-6H sample, which indicates the existence of both Mo_2CT_x and Mo_2Ga_2C and a heterogeneous structure in this sample. With increasing etching time, the (002) peak gradually shifts to lower angles, indicating a continuous expansion of the interlayer spacing due to Ga atom etching. Notably, Mo_2CT_x-12H MXene has the largest interlayer spacing (10.3 Å) and the strongest XRD peak intensity, indicating perfect crystallinity. However, in the case of overetching, as observed for Mo_2CT_x-24H MXene and Mo_2CT_x-36H MXene samples, the (002) characteristic peak gradually shifts to higher angles, and its intensity decreases. The peak shift is caused mainly by functional groups reclosing the already opened interlayer spacing due to overetching. The decrease in peak intensity is attributed to defects introduced into the sample under overettching conditions, leading to a decrease in crystal quality. Indeed, both a significant interlayer spacing and a moderate level of defects enhance the electromagnetic absorption capability of the sample. Therefore, determining the optimal etching process is crucial for constructing high-performance MXene-absorbing materials. In addition, experiments with etching time of 4 and 8 h were also conducted, and XRD patterns are presented in Fig. S1 in the Electronic Supplementary Material (ESM). Both of these samples showed similar semietched states, such as Mo_2CT_x-6H MXene. Thus, this study selected the most representative Mo_2CT_x-6H MXene for further research.

To further illustrate the variation in sample quality under different etching conditions, Raman spectroscopy was performed, as shown in Fig. 2(c), and all the characteristic peaks were consistent with previous studies [34]. The spectra of the Mo_2CT_x MXene clearly show that the characteristic peaks associated with Ga atoms in Mo_2Ga_2C MAX gradually weaken until they disappear after selective etching, especially the characteristic peak at 414 cm^{-1}. Moreover, the peaks at 994.1, 818.2, 281, and 194 cm^{-1}

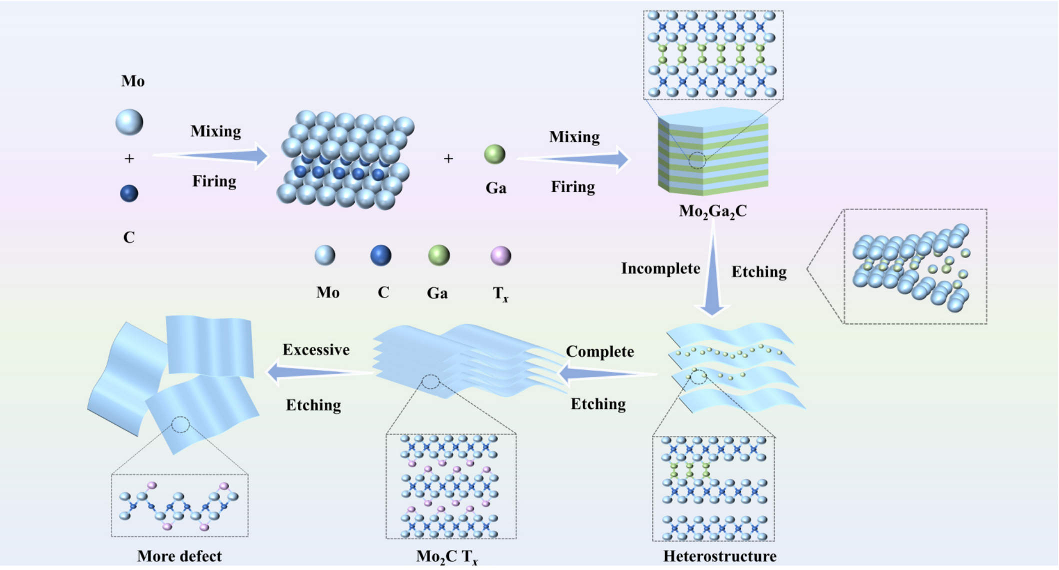

Fig. 1 Fabrication strategy and schematic structure of Mo_2CT_x materials with different etching degrees.

correspond to the A_g^1 and B_{2g} vibrational modes of Mo_2C MXene out-of-plane layer, namely, Mo–C stretching (ν) and bending (δ) vibrations, whereas the 333 cm^{-1} peak in Mo_2CT_x MXene is assigned to Mo–T_x (T_x: –OH, –O, –Cl, and –F) vibrational bonds [35]. The Raman characteristic peaks of the MXene sample are observed to be the sharpest after an etching period of 12 h, indicating the optimal etching quality at this time. However, with increasing etching time, the intensity of Raman peaks gradually decreases due to the introduction of defects caused by prolonged etching. This finding is consistent with XRD results. Moderate defects can enhance a sample's polarization loss capability while reducing its electrical conductivity, indicating a competitive mechanism worthy of further exploration.

The morphology of Mo_2Ga_2C MAX phase is a characteristic layered structure typical of bulk layered materials, as depicted in Fig. 3(a). In contrast, the etched Mo_2CT_x MXene exhibits a finer and differently oriented nanoplate stacking morphology, as illustrated in Figs. 3(b)–3(e). From SEM images, the differences between Mo_2CT_x MXene samples etched to varying extents seem minimal. Figure S2 in the ESM presents EDS mapping images of the Mo_2CT_x-6H MXene, confirming the presence of C, Mo, O, Ga, and F and thus demonstrating partial etching and a heterogeneous structure. Numerous and obvious defects were observed in Mo_2CT_x-36H sample, but Mo_2CT_x-24H MXene and previous samples showed almost no significant defects on the surface, which may be attributed to the impact of acid treatment time on the surface quality of the MXene nanosheets, further indicating that prolonged acid treatment may lead to excessive

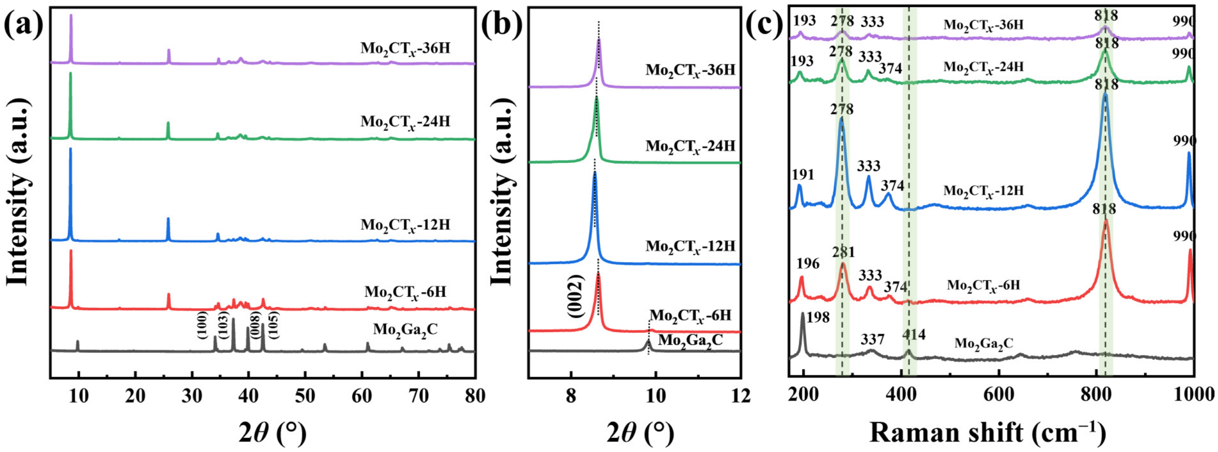

Fig. 2 (a, b) XRD patterns and (c) Raman spectra of Mo_2Ga_2C and Mo_2CT_x MXene with different etching time.

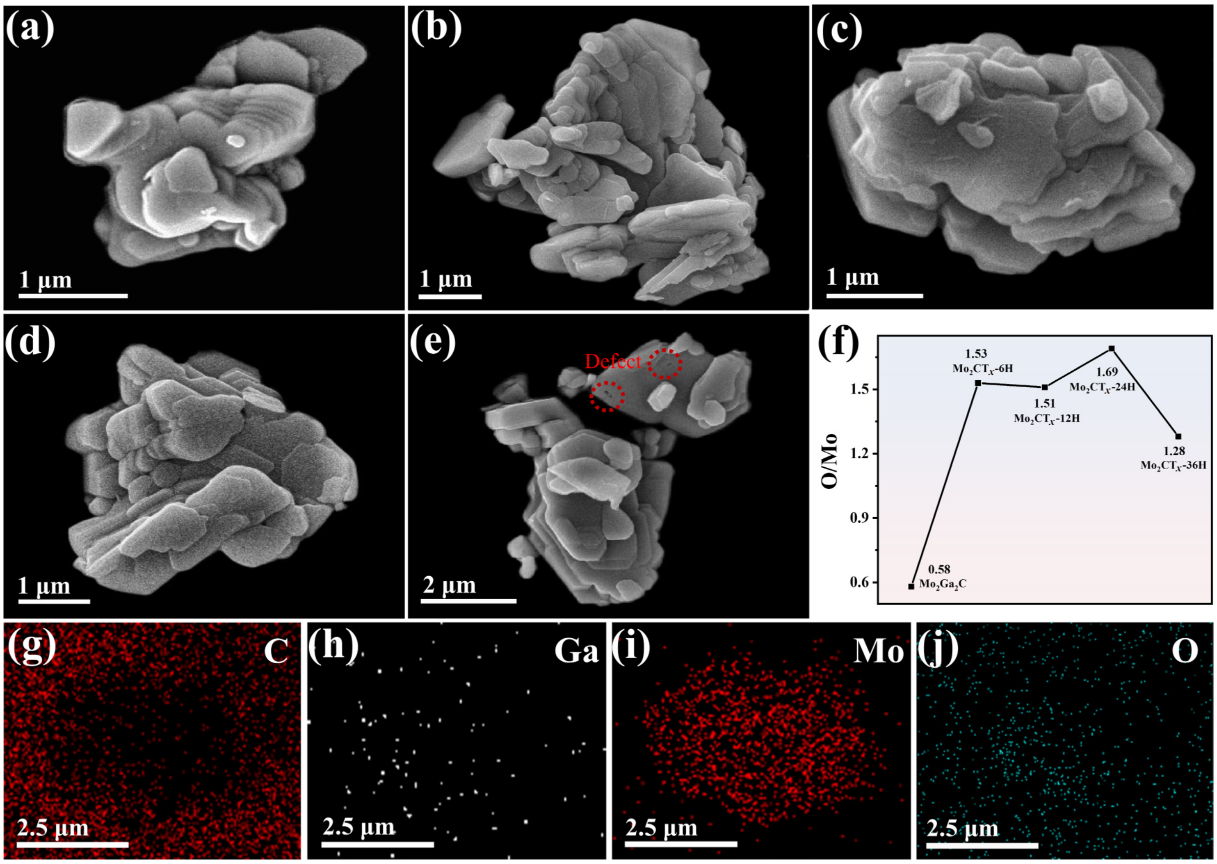

Fig. 3 SEM images of (a) Mo_2Ga_2C, (b) Mo_2CT_x-6H, (c) Mo_2CT_x-12H, (d) Mo_2CT_x-24H, (e) Mo_2CT_x-36H. (f) Average O content and (g–j) EDS element distribution of Mo_2CT_x-12H.

etching of the sample surface. Surface energy spectrum analysis of Mo_2CT_x-12H MXene (Fig. 3(g)–3(j)) revealed a uniform distribution of C, Mo, and O and negligible Ga content, confirming the successful etching of Ga. Mo_2Ga_2C MAX was completely transformed into 2D Mo_2CT_x MXene, with a discernible quantity of oxygen functional groups. To further assess the quality changes of the samples under different etching conditions, the elemental proportion statistics of multiple positions on each sample were obtained, as shown in Fig. S3 in the ESM. The etched Mo_2CT_x terminations primarily feature oxygen functional groups. As the etching time increased to 12 h, the minimal presence of Ga indicates that Ga was successfully etched away. The average O content of each sample is presented in Fig. 3(f), and Mo_2CT_x-24H MXene sample has the highest O content. It can be assumed that the Mo_2CT_x-24H MXene possesses the most O-terminal functional groups, suggesting that more polarization processes are triggered, thus increasing MA properties [36].

The morphology and microstructure of the samples under different etching conditions were further characterized via TEM, high-resolution transmission electron microscopy (HRTEM), and selected area electron diffraction (SAED). In particular, in Fig. 4, the fully etched Mo_2CT_x-12H MXene sample and the overetched Mo_2CT_x-24H MXene sample are presented. Mo_2CT_x-12H MXene nanosheet is shown in Fig. 4(a). Few-layer MXene nanosheets appear as irregular hexagons with a diameter of approximately 400 nm. In addition, SAED pattern (inset of Fig. 4(b)) further confirms the typical hexagonal structure of Mo_2CT_x MXene. HRTEM image of Mo_2CT_x-12H MXene nanosheet in Fig. 4(c) is amplified from the low-magnification HRTEM image in Fig. 4(b). It shows distinct lattice fringes, which indicate high crystallinity in the sample. The interplanar spacing is measured to be 0.26 nm in the upper right corner of Fig. 4(c), which matches well with the (100) crystal plane of Mo_2CT_x MXene. As previously mentioned, Mo_2CT_x MXene is obtained by etching Mo_2Ga_2C and shares the same hexagonal structure and atomic positions on the basal plane; thus, even though the 2D hexagonal crystal does not show an XRD peak at (100), it is believed that the (100) interplanar spacing of 2D Mo_2CT_x measured via TEM is close to the (100) interplanar spacing of Mo_2Ga_2C measured via XRD [37]. TEM image and HRTEM image of Mo_2CT_x-24H MXene nanosheets are shown in Figs. 4(d)–4(f). The diffraction pattern confirms the hexagonal structure of the sample, which indicates that overetching did not alter the structure of Mo_2CT_x. HRTEM image shows a rough surface, revealing an increase in surface defects compared with those of Mo_2CT_x-12H sample. The presence of moderate defects improved the polarization loss ability of the sample to EMW, so excessive etching may also be a good method to enhance the absorption performance. Furthermore, TEM-based EDS mapping analysis of Mo_2CT_x-12H MXene shown in Figs. 4(g)–4(k) further confirms the similar uniform distributions of C, Ga, Mo, and O with SEM-based EDS mapping results.

XPS analysis of Mo_2Ga_2C and Mo_2CT_x samples was performed to investigate the components and chemical bonds, as depicted in Figs. 5(a)–5(d). The full spectra (Fig. 5(a)) analysis reveals that Mo_2Ga_2C MAX phase was mainly composed of Ga, Mo, C, and O, whereas Mo_2CT_x MXene contained only Mo, C, and O, which ultimately indicates that Mo_2Ga_2C MAX phase was successfully converted into Mo_2CT_x MXene. Figure 5(b) shows the high-resolution XPS narrow spectra of Mo 3d; among them, the characteristic peaks at 229.63 and 232.84 eV are mainly attributed

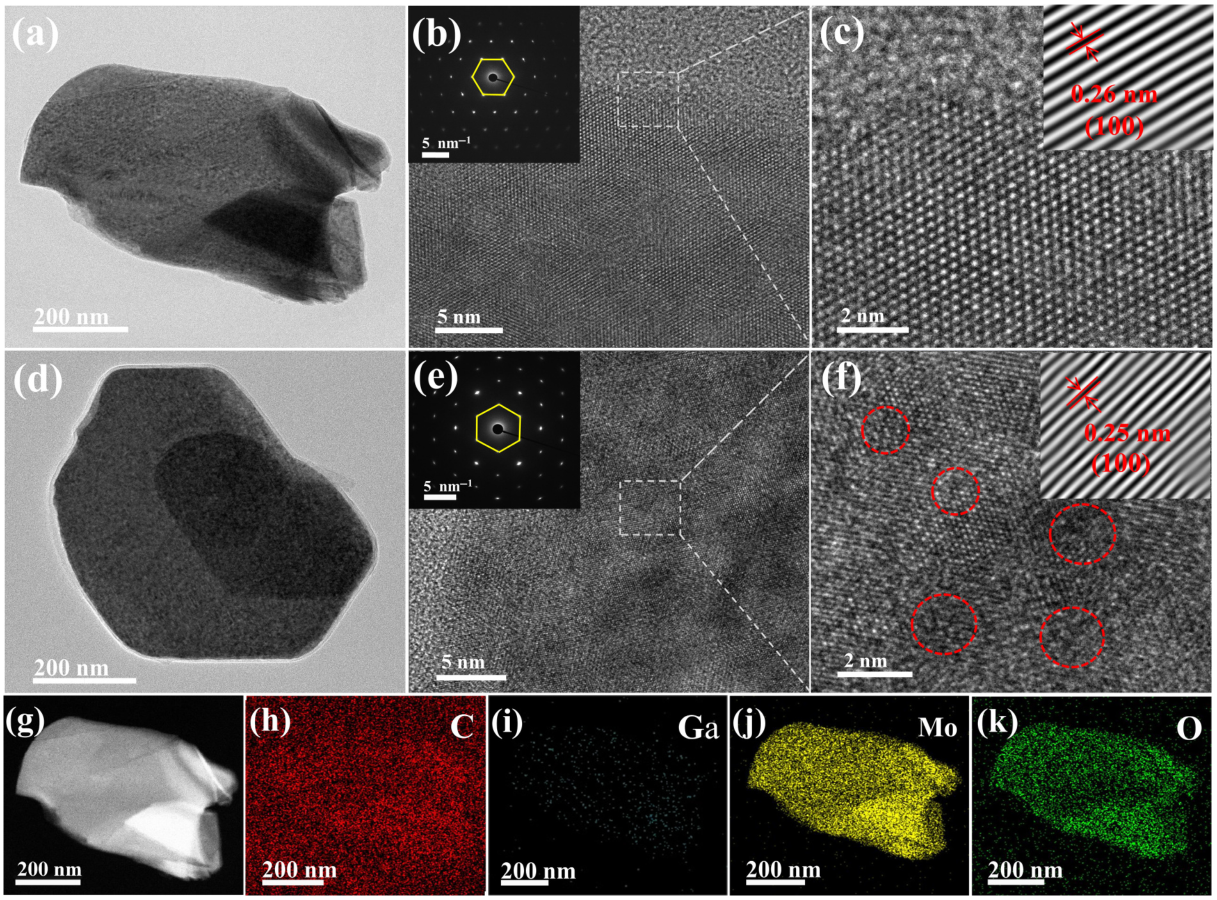

Fig. 4 TEM and HRTEM images (inset: corresponding SAED pattern) of (a–c) Mo_2CT_x-12H and (d–f) Mo_2CT_x-24H; (g–k) EDS spectra of Mo_2CT_x-12H.

to Mo–C, corresponding to Mo–C ($3d_{5/2}$) and Mo–C ($3d_{3/2}$), respectively. The increase in the binding energy of Mo $3d_{5/3}$ suggests that Ga is gradually replaced by surface functional groups (–O, –OH, and/or –F) over time [38]. Notably, the shift of the Mo 3d peak toward a lower binding energy in Mo_2CT_x-36H MXene sample indicates that the atom interaction is weakened due to acid corrosion, which further indicates that the etching time is over-etched after 12 h. Figure 5(c) shows O 1s high-resolution XPS spectra of Mo_2Ga_2C MAX phase and Mo_2CT_x MXene. O 1s peak of Mo_2Ga_2C MAX phase is mainly composed of three parts, Mo–O, Ga–O, and C–O, at 529.73, 530.67, and 532.24 eV, respectively [39]. Furthermore, Ga–O characteristic peak is still observed for the Mo_2CT_x-6H MXene at 530.82 eV. As the etching time increases, Ga–O bond is gradually broken due to the removal of Ga, accompanied by the disappearance of Ga–O peak. The broken O single bonds bind to Mo_2C to form new functional groups (–O, –OH), and Mo–O moves toward higher binding energies. In addition, C 1s spectra display two peaks near 284.8 and 283.7 eV attributed to C–C and C–Mo bonds, respectively (Fig. 5(d)) [40]. In particular, both the binding energy and the peak area of C-Mo bond gradually decrease as the etching time increases, which indicates that C-Mo bond is gradually broken due to the influence of acid corrosion during the etching process, leading to more C single bonds forming C-O bonds with O, further suggesting an increase in O functional groups on the surface. The high-resolution XPS spectra of Ga 3d are shown in Fig. S4 in the ESM, where the peaks at 19.3 and 20.52 eV belong to metallic Ga and Ga oxide, respectively [41]. As the etching process progresses, Ga peak gradually disappears, indicating the transformation from Mo_2Ga_2C to Mo_2CT_x.

Additionally, Fig. 5(e) displays N_2 adsorption–desorption isotherm at 77 K, which is classified according to IUPAC (International Union of Pure and Applied Chemistry) [42]. All the isotherms are type III (reversible adsorption–desorption curves) and show no obvious hysteresis loop in the high-pressure range. Moreover, SSAs of Mo_2Ga_2C, Mo_2CT_x-6H, Mo_2CT_x-12H, Mo_2CT_x-24H, and Mo_2CT_x-36H MXene were calculated to be 4.68, 6.41, 7.89, 7.56, and 7.67 $m^2 \cdot g^{-1}$, respectively, when the relative pressure P/P_0 was 0.99. The variation trend of SSA results was opposite to that of the surface oxygen content on the surface. At the beginning of the etching process, as time increases, the surface oxide is etched away first, and SSA gradually increases. When the etching time exceeds 12 h, overetching makes it easier for the surface to combine with functional groups, the number of oxygen functional groups increases, and the interlayer spacing decreases, leading to a decrease in SSA. When the etching time continues to increase to 36 h, the oxygen functional groups gradually break under the strong corrosion of hydrochloric acid, the surface structure is damaged, and more defects appear, thus, SSA increases again. In this scenario, the interactions between Mo_2C interlayer and surface functional groups (–O, –OH), as well as increasing sample defects, play crucial roles in MA performance.

3.2 MA performance of Mo_2CT_x MXene

MA performance of the prepared samples depends on their

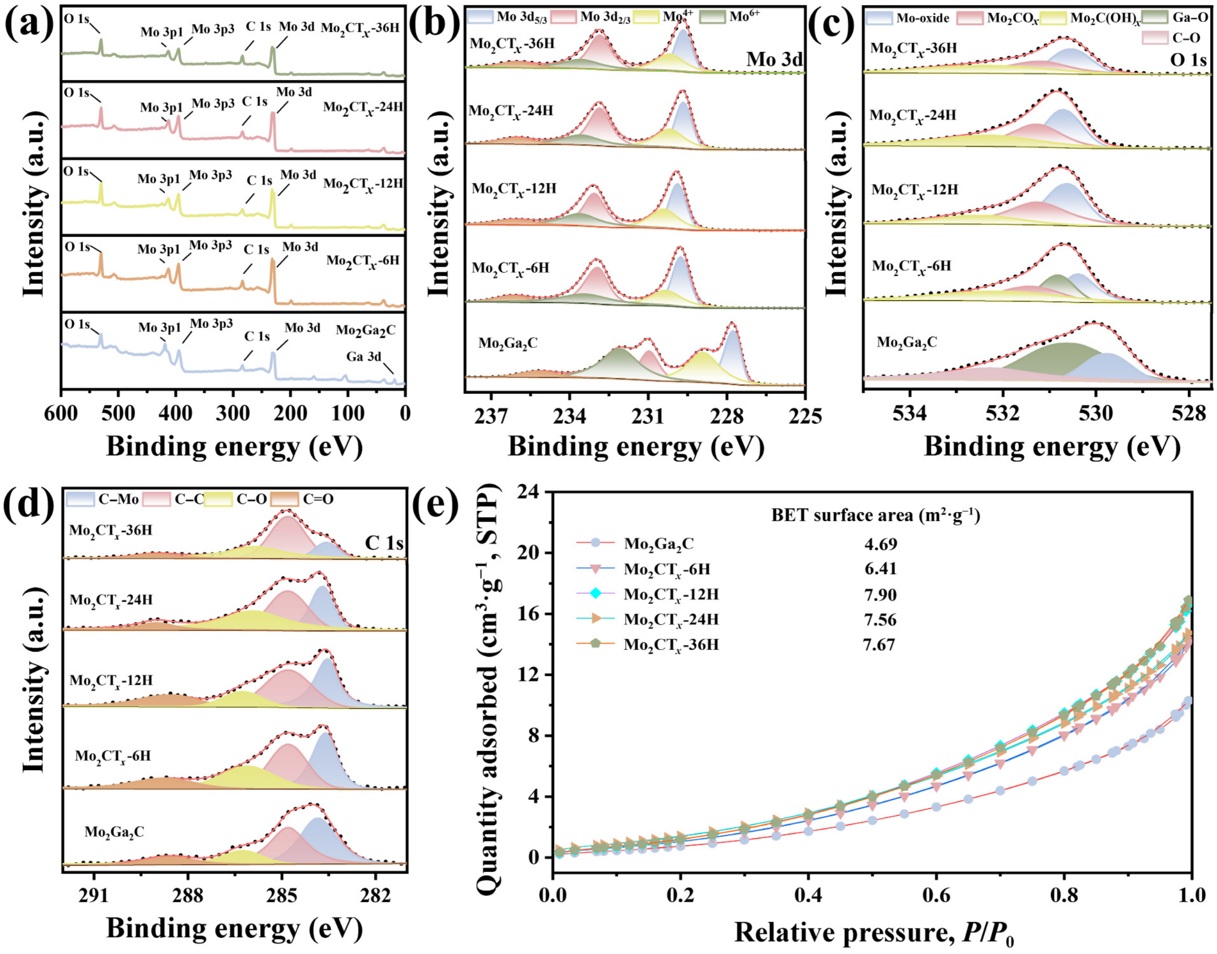

Fig. 5 (a, b) Mo 3d, (c) O 1s, and (d) C 1s high-resolution XPS narrow spectra. (e) N_2 adsorption isotherms of Mo_2Ga_2C and Mo_2CT_x MXene.

electromagnetic parameters, complex dielectric parameters ($\varepsilon_r = \varepsilon' - j\varepsilon''$) and magnetic permeability ($\mu_r = \mu' - j\mu''$) [43], as plotted in Fig. 6. MA performance of nonmagnetic-prepared samples mainly lies in their permittivity rather than their permeability [44]. The real parts (ε') and imaginary parts (ε'') of the permittivity represent the storage and attenuation capacities of the EMW, as shown in Figs. 6(a) and 6(b), respectively [45]. ε' and ε'' present a decreasing variation trend accompanied by increasing frequency overall. Meanwhile, some slight fluctuations are also observed in the curves. According to free electron theory, as expressed in Eq. (3) [46]:

$$\varepsilon'' = \sigma(2\pi f \varepsilon_0)^{-1} \tag{3}$$

where ε_0 represent the permittivity of free space. The dielectric loss factor (ε'') is positively correlated with conductivity (σ) [47]. This relationship indicates that a higher conductivity of materials leads to an increase in the dielectric loss factor. As shown in Fig. 6(d), the Mo_2Ga_2C MAX phase has a high ε'' value because of its excellent conductivity, indicating a strong EMW absorption capability. However, as Ga content decreases, the dielectric constant (ε'') and dielectric loss factor (ε'') of Mo_2CT_x-6H MXene significantly decrease. This reduction may be attributed to the decrease in conductivity caused by the lower Ga content, which reduces the freedom of electrons and thus lowers the overall conductivity and dielectric loss of the materials. When the etching time was increased to 12 h, ε' and ε'' values of Mo_2CT_x-12H MXene sample began to rise because of the expansion of the interlayer spacing caused by the etching process. This phenomenon suggests that an increase in the interlayer spacing may enhance the material's EMW absorption ability, as a larger interlayer spacing may provide a longer path for EMW to propagate within the materials, thereby improving the absorption effect. Further extending the etching time to 24 h resulted in a continued increase in ε' and ε'' values for Mo_2CT_x-24H MXene sample, accompanied by noticeable curve fluctuations. This variation can be attributed to the presence of numerous defects and a high density of surface functional groups in the sample. Extended etching introduces more defects and surface functional groups, which can trigger additional polarization effects and conductive losses, thereby increasing the overall dielectric loss of the materials. In general, in this study, the dielectric loss of Mo_2CT_x MXene is mainly due to the synergistic effects of conductive loss and polarization loss. Conductive loss arises from the movement and scattering of free electrons within a material, whereas polarization loss is related to the polarization processes within the materials. The combined effects of these factors determine the material's EMW absorption performance [48,49]. Figure 6(c) shows the dielectric loss tangent ($\tan\delta_\varepsilon = \varepsilon''/\varepsilon'$); among them, Mo_2CT_x-24H MXene has the highest $\tan\delta_\varepsilon$ value, implying a superior dielectric loss capability. In addition, there are obvious fluctuations in the dielectric loss curve of Mo_2CT_x-24H MXene because of the resonance phenomenon [50]. In addition, the conductivity of the prepared samples was determined and is shown in Fig. 6(d). Notably, the conductivity first tends to increase but then decreases and then increases again with increasing

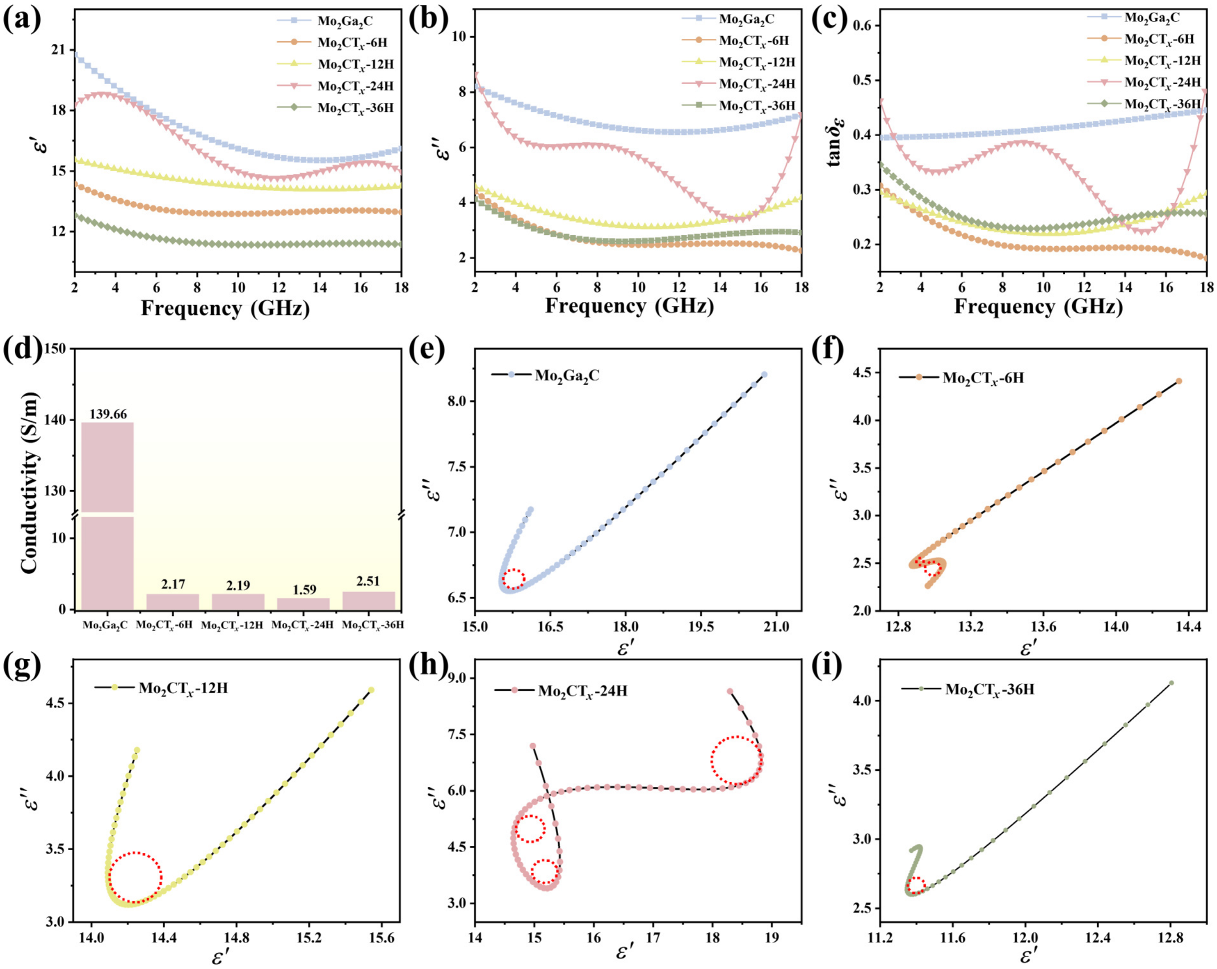

Fig. 6 Electromagnetic parameters of prepared samples: (a) ε', (b) ε'', (c) tanδ, (d) conductivity, and (e–i) Cole–Cole circles.

etching time. The reasons for the change in conductivity during the etching process may involve several factors. Some surface oxides are removed after etching for 12 h, which leads to smoother electron transport. Nevertheless, excessive etching (24 h) results in damage to the layer structure of Mo_2C and an increase in the number of surface functional groups, thus hindering electron transport. Afterwards, when the etching time increased to 36 h, some damaged layer structures were realigned, or the surface became clean, achieving smooth electron transport again and a renewed increase in conductivity.

The Cole–Cole circle diagrams based on Debye theory (Eq. (4)) are displayed in Figs. 6(e)–6(i):

$$\left(\varepsilon' - \frac{\varepsilon_s + \varepsilon_\infty}{2}\right)^2 + (\varepsilon'')^2 = \left(\frac{\varepsilon_s - \varepsilon_\infty}{2}\right)^2 \tag{4}$$

where ε_s and ε_∞ represent the static dielectric constant and relative dielectric constant at the high-frequency limit, respectively. There are no less than one irregular semicircle, demonstrating that multiple Debye relaxation processes occurred in all the samples [51]. Evidently, Mo_2CT_x-12H MXene sample has a larger semicircle than the other microwave absorbers do, indicating an enhanced polarization loss process and multiple relaxation processes [52]. In addition, the long tail also contributes to excellent conduction loss [53]. An increasing number of regular semicircles are observed in Mo_2CT_x-24H MXene, indicating the existence of more interfaces, defects, and chemical bonds [44], which contribute to satisfactory MA performance.

Three-dimensional (3D) images were used to demonstrate MA ability of different samples with thicknesses of 1–5 mm. As shown in Figs. 7(a)–7(e), the minimum reflection loss (RL_{min}) value of Mo_2Ga_2C MAX is −16.2 dB at 15.7 GHz with a thickness of 1.3 mm, which indicates weak electron absorption ability. With the removal of Ga, there is an obvious improvement in EMW absorption performance of Mo_2CT_x MXene, which can be seen directly from Mo_2CT_x-6H MXene RL value of −33.9 dB. Mo_2CT_x-12H MXene achieves an RL_{min} value of −44.4 dB in thickness, and a satisfactory EAB covers 4.4 GHz (13.42–17.82 GHz) with a thickness of only 1.3 mm. For Mo_2CT_x-24H MXene, the optimum EMW absorption ability of −60.7 dB is obtained at 1.5 mm, and EAB reaches 3.98 GHz (13.85–17.83 GHz), with a thickness of only 1.2 mm. The functional group content (–O, –OH) and surface defects enhanced the dielectric properties and polarization of the MXene, thus increasing EMW absorption performance of the samples. However, as the etching time further increased to 36 h, RL_{min} value decreased to −24.8 dB with a terrible thickness of 5 mm. The continuous increase in defects does not necessarily result in better MA performance, and a low oxygen content leads to weak performance. Hence, it is important to achieve a balance between the number of functional groups and the number of defects for optimum MA performance, which further demonstrates that it is feasible to modulate the performance by adjusting the etching time. A comparison of RL curves at 1.5 mm (Fig. 7(f)) shows that Mo_2CT_x-24H MXene has an RL_{min} value with the same thickness, achieving the best MA performance.

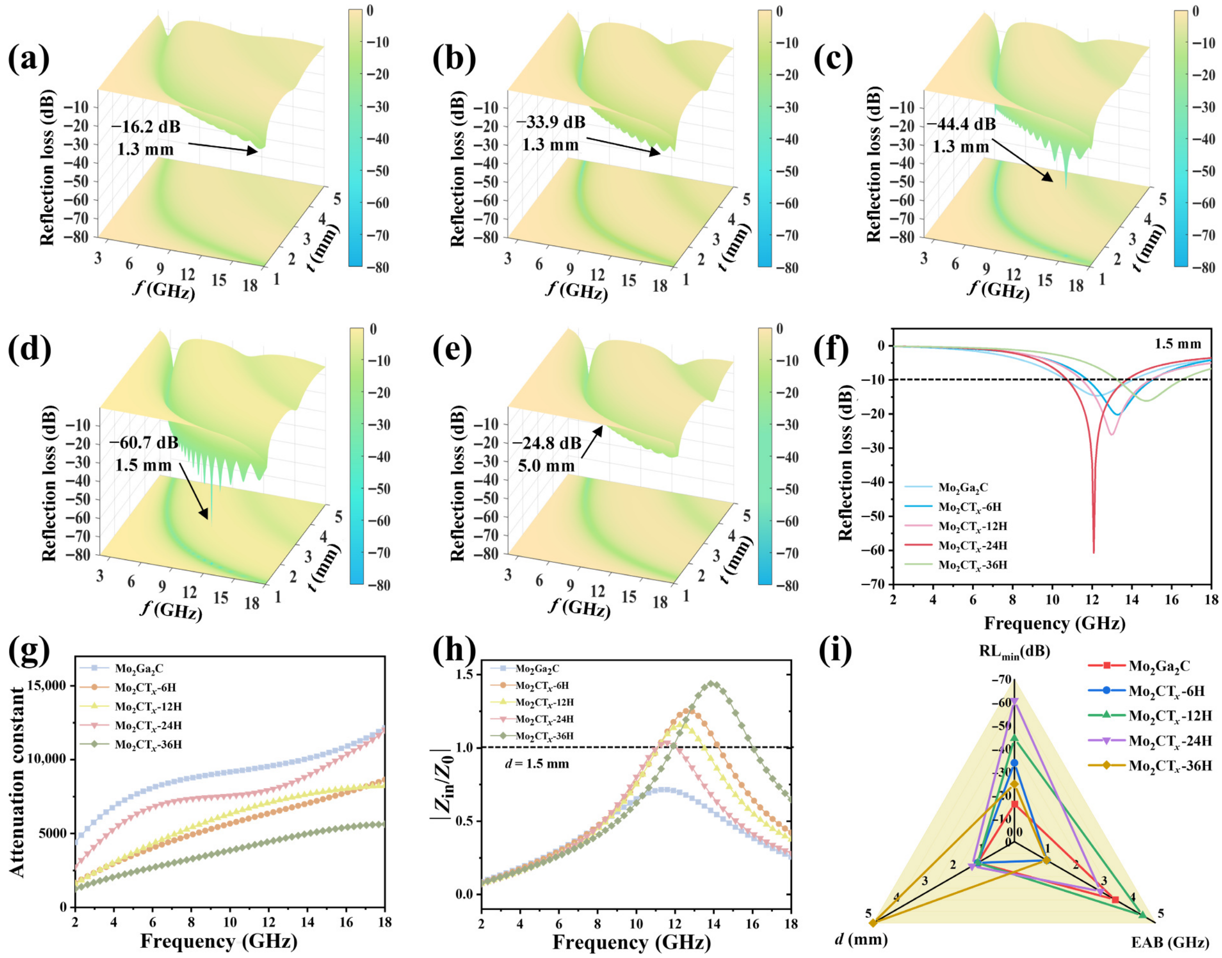

Fig. 7 3D RL value plots of (a) Mo_2Ga_2C MAX, (b) Mo_2CT_x-6H, (c) Mo_2CT_x-12H, (d) Mo_2CT_x-24H, and (e) Mo_2CT_x-36H vs. frequency and sample thickness. (f) Comparison of RL curves at 1.5 mm, (g) α, (h) Z_{in}/Z_0, and (i) radar comparison plot of EMW absorption performance.

To evaluate the capacity to dissipate EM waves, the attenuation constant (α) is calculated via Eq. (5):

$$\alpha=\frac{\sqrt{2}\pi f}{c}\times\sqrt{(\mu''\varepsilon''-\mu'\varepsilon')+\sqrt{(\mu''\varepsilon''-\mu'\varepsilon')^2+(\mu''\varepsilon'+\mu'\varepsilon'')^2}} \tag{5}$$

where f is the frequency, and c represents the velocity of light in free space. The frequency dependence of α for the prepared absorbers is plotted in Fig. 7(g). α values of all five samples increased significantly with increasing frequency ranging from 2–18 GHz, suggesting better EM wave dissipation potential in the higher frequency range. Among them, Mo_2Ga_2C MAX phase has the highest α values because of its optimum conductivity. However, given the impedance mismatch, Mo_2Ga_2C does not exhibit the theoretical best MA performance. Notably, Mo_2CT_x-24H MXene has a dissipation capability second to that of Mo_2Ga_2C MAX phase, and α value exceeds 2500, which is attributed to its enhanced polarization relaxation and conductive loss abilities.

Effective impedance matching is another crucial factor affecting optimum absorption performance [54,55]. The relationship between the characteristic impedance ($Z = |Z_{in}/Z_0|$) and frequency is depicted in Fig. 7(h) to further elucidate the impact of absorbers on EMW absorption performance. Typically, when Z_{in} value is close to Z_0, i.e., Z = 1, the incident EM waves can enter MA materials entirely without reflection in theory [56]. Mo_2CT_x-24H MXene clearly possesses the optimum impedance matching at a thickness of 1.5 mm. The decreased conductive loss and enhanced polarization process caused by the lower conductivity and abundant surface defects, respectively, optimize the impedance matching of the absorber. On the basis of the synergistic effect of the above two factors of impedance matching and the attenuation constant, Mo_2CT_x-24H MXene has the optimum RL_{min}. An overall comparison of EMW absorption performance of different samples is depicted intuitively in Fig. 7(i). The Mo_2CT_x-24H MXene has the optimum RL_{min} value of −60.7 dB (1.5 mm), whereas Mo_2CT_x-12H MXene has a superior EAB of 4.4 GHz (1.3 mm). Therefore, the modulation of surface defects by a reasonable adjustment of the etching time is an effective strategy for tailoring the electromagnetic parameters and enhancing MA ability.

The relationship between the absorber thickness and the absorption peak frequency corresponding to different RL_{min} values of Mo_2CT_x-24H MXene is given in Fig. 8(a). According to Eq.(6):

$$d_m=\frac{n\lambda_m}{4}=\frac{nc}{4f_m\sqrt{|\varepsilon_r\mu_r|}}(n=1,\ 3,\ 5,\ldots) \tag{6}$$

where d_m and f_m represent the optimum thickness and frequency of the RL_{min} peak, respectively, and λ_m represents the microwave wavelength corresponding to f_m. The red triangle symbolizes the specific thickness at t_m, whereas the black curve represents the calculated theoretical thickness. All "red triangular marks" clearly fall on the dark curve, suggesting that RL_{min} values of Mo_2CT_x-24H MXene with different thicknesses correspond to the same frequency as the $\lambda/4$ curve of the corresponding thickness, which demonstrates that the absorption mechanism of Mo_2CT_x-24H MXene adheres to $\lambda/4$ principle. Moreover, RL_{min} peak gradually moves in the low-frequency direction with increasing absorber thickness, which is one of the important characteristics of the quarter-wavelength matching model. In other words, when EMW enters the absorber, destructive interference occurs when the phase difference between the two reflected waves is $\lambda/4$ due to the existence of numerous interfaces, thus enhancing the loss ability of EMW [57,58]. Generally, the ideal absorber achieves a lower RL value and a wider EAB at a thin material thickness. To evaluate the competitiveness of the prepared samples, MA performance of Mo_2CT_x-12H and Mo_2CT_x-24H MXene was comprehensively compared with that of other previously reported MXene-based absorbers in terms of RL, EAB, and material thickness (Fig. 8(b) and detailed in Table S1 in the ESM). Mo_2CT_x demonstrates superior performance among all single-phase MXene absorbers, achieving excellent EMW absorption properties comparable to those of MXene-based composite absorbers without the need for complex composite processes or structural designs. Particularly notable is its ability to achieve −60.7 dB RL and a 4.4 GHz EAB even at ultrathin thicknesses. Compared with the other samples, Mo_2CT_x MXene not only exhibit a superior RL but also maintain

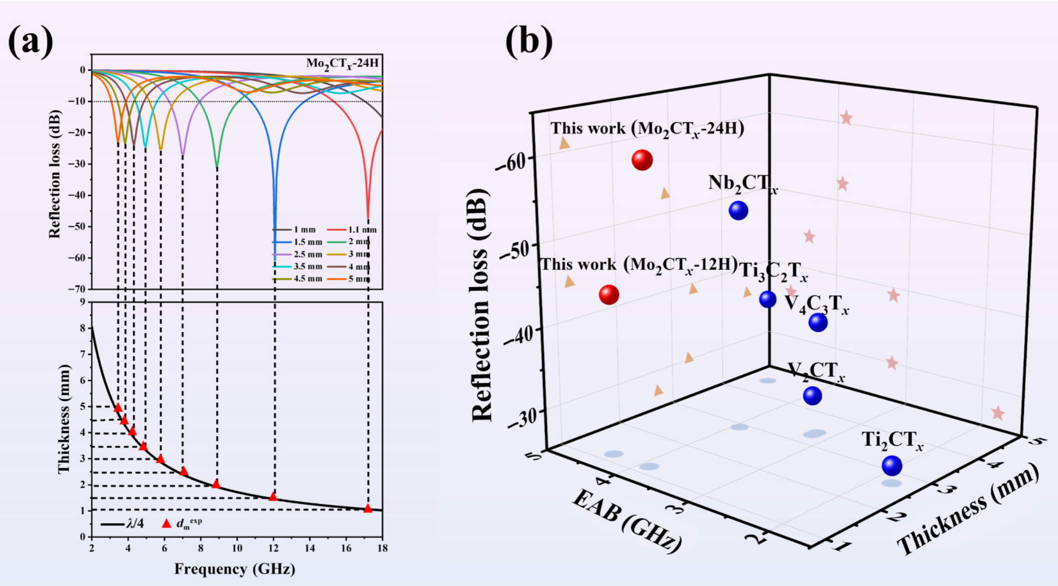

Fig. 8 (a) Minimum RL curves and relevant $\lambda/4$ matching model of Mo_2CT_x-24H MXene. (b) Comparison of EMW absorption performance with that of other reported pure MXene absorbers [30, 59–62].

a relatively high EAB. This indicates that Mo_2CT_x MXene can achieve strong EMW absorption while effectively absorbing EMW across a broad frequency range, thereby enhancing their overall performance and application potential as EMW absorption materials.

3.3 EMW absorption mechanism of Mo_2CT_x

Figure 9 summarized the EMW absorption mechanism of Mo_2CT_x MXene. First, after etching treatment, the inherent functional groups on the MAX phase surface are transformed into higher-activity sites, which facilitates the accumulation of dipoles within the materials. Specifically, the etching process removes some inactive surface materials, generating more active sites and thus more effectively promoting the polarization of dipoles, which leads to a more uneven charge distribution, increasing EMW absorption ability and thereby enhancing MA performance [63]. Second, the presence of oxygen-containing functional groups on the MXene surface is a key factor in promoting the formation of conductive pathways. These oxygen functional groups interact with MXene surface to create new conductive channels, significantly improving electron mobility. Although these conductive channels facilitate electron migration, they also increase conductive loss due to the presence of additional scattering centers, which reduces the material's overall electrical conductivity. Third, the multilayer structure of MXene effectively extends the transmission path of the EMW. In this structure, EMWs undergo multiple scattering and reflection events, resulting in the attenuation of wave energy within the materials. This multilayered scattering mechanism significantly enhances the ability of materials to absorb EMW, as each scattering and reflection mechanism increases the residence time of the waves within the materials, improving wave attenuation. Additionally, the abundant defects and interfaces introduced by etching create various interfacial polarization processes. These defects and interfaces provide more opportunities for wave polarization, increasing the diversity and complexity of the polarization process, which further improves the material's EMW absorption performance. This diverse polarization mechanism not only enhances the material's absorption capacity but also improves its absorption efficiency. Finally, the balance between conductive loss and polarization processes optimizes the impedance matching of the materials. By precisely adjusting this balance, we achieve optimal EMW absorption, meaning that EMWs are effectively dissipated upon entering the materials and that the reflected waves are minimized. This optimization allows Mo_2CT_x MXene to exhibit excellent MA performance, indicating its high potential for applications in MA [53].

4 Conclusions

In summary, Mo_2CT_x MXene with various etching time were

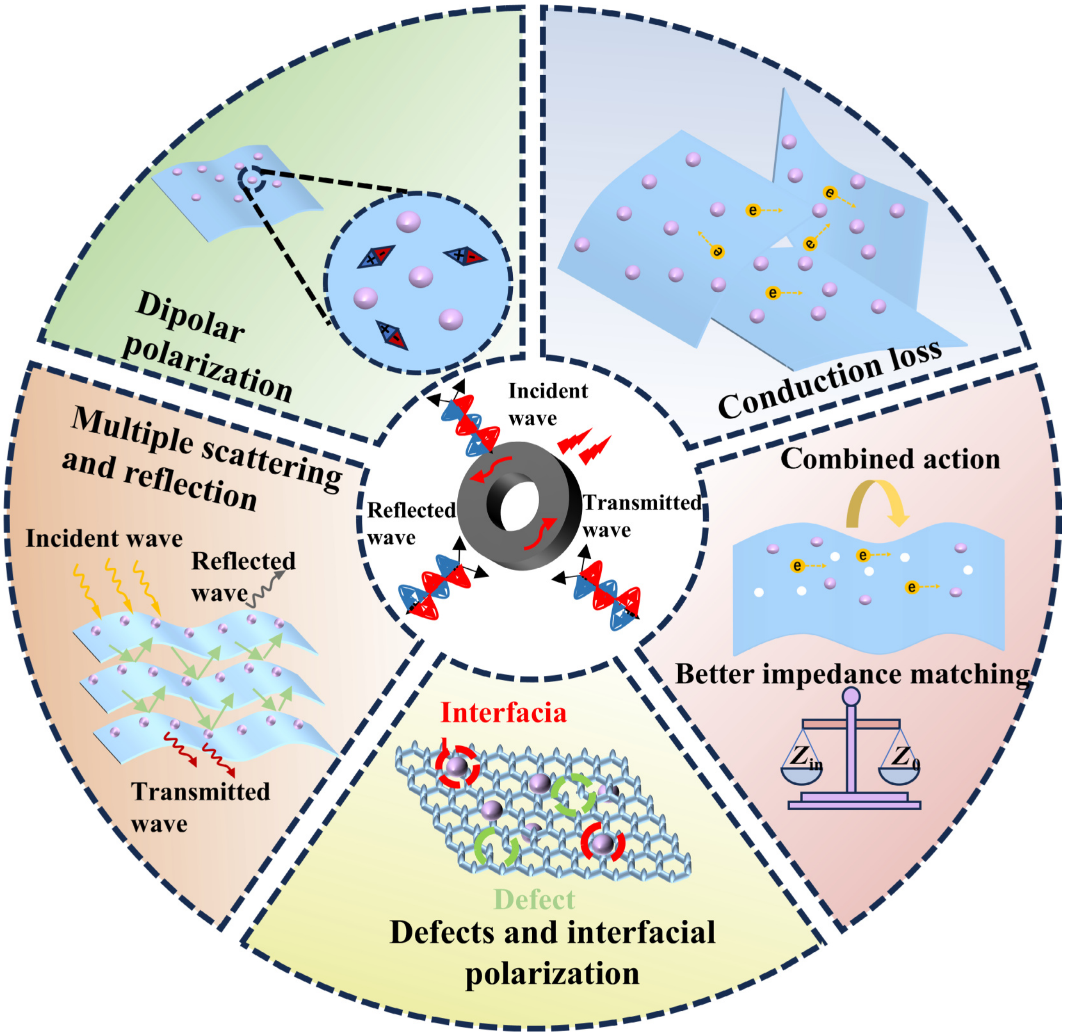

Fig. 9 Schematic illustration of EMW absorption mechanism of Mo_2CT_x MXene.

synthesized via a direct hydrothermal etching method, followed by an investigation into the impact of different etching degrees on MA capacity. More importantly, the content of oxygen functional groups and defects generated by etching are key factors in the impedance matching of the absorption materials. Benefiting from synergistic EMW absorption mechanisms, including dipole polarization, multiple interfacial polarizations and conductive losses caused by defects and oxygen functional groups, and multiple scattering and reflections caused by a multilayered structure, Mo_2CT_x-12H MXene achieves an RL_{min} value of −44.4 dB, a broad EAB of 4.4 GHz, and a thickness of only 1.3 mm. RL_{min} value of Mo_2CT_x-24H MXene is −60.7 dB at a thickness of 1.5 mm, and EAB reaches 3.98 GHz at a thickness of 1.2 mm. Overall, this work provides a feasible strategy for tailoring Mo-based MXene absorbers to achieve ideal MA properties. Furthermore, Mo_2CT_x demonstrates the highest absorption performance among all the pure MXenes, suggesting that it could become a focal point for researching the next generation of MXene-based absorption materials.

Acknowledgements

We thank the National Natural Science Foundation of China (Nos. 52202364, 52372284, and 52275187), the Key Scientific Research Project of Colleges and University in Henan Province (No. 24A430019), the Natural Science Foundation of Henan (No. 232300421135), the Fundamental Research Funds for the Universities of Henan Province (No. NSFRF200101), the Henan Province Key Science and Technology Research Projects (No. 242102230097), and the Doctoral Fund Project of Henan Polytechnic University (No. B2023-18). This work is also supported by the Hebei Key Laboratory of Dielectric and Electrolyte Functional Material, Northeastern University at Qinhuangdao (No. HKDEFM2023103), and the Science and Technology Project of the Hebei Education Department (No. QN2023235).

Declaration of competing interest

The authors have no competing interests to declare that are relevant to the content of this article. The author Aiguo Zhou is the Editorial Committee member of this journal.

Electronic Supplementary Material

Supplementary material is available in the online version of this article at https://doi.org/10.26599/JAC.2024.9220977.

References

[1] Zeng XJ, Jiang X, Ning Y, *et al.* Constructing built-in electric fields with semiconductor junctions and Schottky junctions based on Mo–MXene/Mo–metal sulfides for electromagnetic response. *Nano-Micro Lett* 2024, **16**: 213.

[2] Pang HF, Duan YP, Huang LX, *et al.* Research advances in composition, structure and mechanisms of microwave absorbing materials. *Compos Part B Eng* 2021, **224**: 109173.

[3] Wang Y, Gao X, Fu YQ, *et al.* Enhanced microwave absorption performances of polyaniline/graphene aerogel by covalent bonding. *Compos Part B Eng* 2019, **169**: 221–228.

[4] Song CQ, Yin XW, Han MK, *et al.* Three-dimensional reduced graphene oxide foam modified with ZnO nanowires for enhanced microwave absorption properties. *Carbon* 2017, **116**: 50–58.

[5] Jiang JL, Zhao WC, Zhao L. Ultrarapid gelation of porous $Ti_3C_2T_x$ MXene monoliths induced by ionic liquids. *Nano Lett* 2024, **24**: 3196–3203.

[6] Zhu YC, Rajouâ K, Le Vot S, *et al.* Modifications of MXene layers for supercapacitors. *Nano Energy* 2020, **73**: 104734.

[7] Liang CB, Qiu H, Song P, *et al.* Ultra-light MXene aerogel/wood-derived porous carbon composites with wall-like “mortar/brick” structures for electromagnetic interference shielding. *Sci Bull* 2020, **65**: 616–622.

[8] Fan JC, Yang RS, Du YQ, *et al.* A triboelectric nanogenerator based on MXene/TPU composite films with excellent stretchability for self-powered flexible sensing. *Nano Energy* 2024, **129**: 109999.

[9] Guo YT, Zhang X, Jin S, *et al.* Synthesis of Mo_2C MXene with high electrochemical performance by alkali hydrothermal etching. *J Adv Ceram* 2023, **12**: 1889–1901.

[10] Qiao LJ, Bi JQ, Liang GD, *et al.* Synthesis of high-entropy MXenes with high-efficiency electromagnetic wave absorption. *J Adv Ceram* 2023, **12**: 1902–1918.

[11] Karataş Y, Çetin T, Akinay Y, *et al.* Synthesis and characterization of Pd doped MXene for hydrogen production from the hydrolysis of methylamine borane: Effect of cryogenic treatment. *J Energy Inst* 2023, **109**: 101310.

[12] Ulas B, Çetin T, Kaya Ş, *et al.* Novel $Ti_3C_2X_2$ MXene supported $BaMnO_3$ nanoparticles as hydrazine electrooxidation catalysts. *Int J Hydrogen Energ* 2024, **58**: 726–736.

[13] Zhang X, Zhang ZH, Zhou Z. MXene-based materials for electrochemical energy storage. *J Energy Chem* 2018, **27**: 73–85.

[14] Cui GZ, Zheng X, Lv XL, *et al.* Synthesis and microwave absorption of $Ti_3C_2T_x$ MXene with diverse reactant concentration, reaction time, and reaction temperature. *Ceram Int* 2019, **45**: 23600–23610.

[15] Du YQ, Yan ZK, You WB, *et al.* Balancing MXene surface termination and interlayer spacing enables superior microwave absorption. *Adv Funct Mater* 2023, **33**: 2301449.

[16] Liu Y, Zhao YB, Ma CT, *et al.* Ultralow-content Co decoration on $Ti_3C_2T_x$ MXene induced electromagnetic characteristic modulation for efficient microwave absorption. *Ceram Int* 2024, **50**: 24406–24416.

[17] Li N, Xie X, Lu HX, *et al.* Novel two-dimensional $Ti_3C_2T_x$/Ni-spheres hybrids with enhanced microwave absorption properties. *Ceram Int* 2019, **45**: 22880–22888.

[18] Zhou CL, Wang XX, Luo H, *et al.* Interfacial design of sandwich-like CoFe@$Ti_3C_2T_x$ composites as high efficient microwave absorption materials. *Appl Surf Sci* 2019, **494**: 540–550.

[19] Kong L, Qi J, Li MH, *et al.* Electromagnetic wave absorption properties of $Ti_3C_2T_x$ nanosheets modified with *in situ* growth carbon nanotubes. *Carbon* 2021, **183**: 322–331.

[20] Zhu WJ, Ye F, Li MH, *et al.* *In-situ* growth of wafer-like Ti_3C_2/carbon nanoparticle hybrids with excellent tunable electromagnetic absorption performance. *Compos Part B Eng* 2020, **202**: 108408.

[21] Wang Y, Dou Q, Jiang W, *et al.* $Ti_3C_2T_x$ MXene beaded SiC nanowires for efficient microwave absorption. *ACS Appl Nano Mater* 2022, **5**: 9209–9222.

[22] Li X, Wen CY, Yang LT, *et al.* Enhanced visualizing charge distribution of 2D/2D MXene/MoS_2 heterostructure for excellent microwave absorption performance. *J Alloys Compd* 2021, **869**: 159365.

[23] Zhang HY, Ji H, Dai GL, *et al.* Nanoarchitectonics of integrated impedance gradient MXene/PPy/polyester composite fabric for enhanced microwave absorption performances. *Compos Part A Appl S* 2022, **163**: 107163.

[24] Han MK, Shuck CE, Singh A, *et al.* Efficient microwave absorption with $V_{n+1}C_nT_x$ MXenes. *Cell Rep Phys Sci* 2022, **3**: 101073.

[25] Miao BJ, Cao YG, Zhu QS, *et al.* Scalable synthesis of 2D Ti_2CT_x MXene and molybdenum disulfide composites with excellent microwave absorbing performance. *Adv Compos Hybrid Mater* 2023, **6**: 61.

[26] Song SW, Liu JQ, Zhou CL, *et al.* Nb_2O_5/Nb_2CT_x composites with different morphologies through oxidation of Nb_2CTx MXene for high-performance microwave absorption. *J Alloys Compd* 2020, **843**: 155713.

[27] Kumaravel V, Rhatigan S, Mathew S, *et al.* Mo doped TiO_2: Impact

on oxygen vacancies, anatase phase stability and photocatalytic activity. *J Phys Mater* 2020, **3**: 025008.

[28] He WY, Zheng XJ, Peng JF, *et al.* Mo-dopant-strengthened basal-plane activity in VS_2 for accelerating hydrogen evolution reaction. *Chem Eng J* 2020, **396**: 125227.

[29] Hu FY, Wang XH, Niu HH, *et al.* Synthesis and electromagnetic wave absorption of novel $Mo_2TiC_2T_x$ MXene with diverse etching methods. *J Mater Sci* 2022, **57**: 7849–7862.

[30] Yang K, Cui YH, Wan LY, *et al.* Preparation of three-dimensional Mo_2C/NC@MXene and its efficient electromagnetic absorption properties. *ACS Appl Mater Inter* 2022, **14**: 7109–7120.

[31] Guo TJ, Chang SQ, Akinay Y. Synthesis of PPy@$Ba_{0.5}Sr_{0.5}Fe_{12}O_{19}$/CNFs by reverse *in situ* polymerization method for microwave absorption applications. *Synthetic Met* 2020, **266**: 116387.

[32] Jin S, Su TC, Hu QK, *et al.* Thermal conductivity and electrical transport properties of double-A-layer MAX phase Mo_2Ga_2C. *Mater Res Lett* 2020, **8**: 158–164.

[33] Zhang YM, Wei JX, Jia MY, *et al.* *In situ* construction of accordion-like nano MoS_2@multilayered Mo_2CT_x hybrid framework toward sodium ion capacitors. *ACS App Energy Mater*2024, **3**:02898.

[34] Min J, Wang KY, Liu J, *et al.* Facile synthesis of uniform MoO_2/Mo_2CT_x heteromicrospheres as high-performance anode materials for lithium-ion batteries. *J Power Sources* 2017, **363**: 392–403.

[35] Kim H, Anasori B, Gogotsi Y, *et al.* Thermoelectric properties of two-dimensional molybdenum-based MXenes. *Chem Mater* 2017, **29**: 6472–6479.

[36] Gong CC, Ding JW, Wang CX, *et al.* Defect-induced dipole polarization engineering of electromagnetic wave absorbers: Insights and perspectives. *Compos Part B Eng* 2023, **252**: 110479.

[37] Guo YT, Jin S, Wang LB, *et al.* Synthesis of two-dimensional carbide Mo_2CT_x MXene by hydrothermal etching with fluorides and its thermal stability. *Ceram Int* 2020, **46**: 19550–19556.

[38] Halim J, Cook KM, Naguib M, *et al.* X-ray photoelectron spectroscopy of select multi-layered transition metal carbides (MXenes). *Appl Surf Sci* 2016, **362**: 406–417.

[39] Jabbarvand Behrouz S, Khataee A, Vatanpour V, *et al.* Surface bioengineering of Mo_2Ga_2C MAX phase to develop blended loose nanofiltration membranes for textile wastewater treatment. *ACS Appl Mater Inter* 2024, **16**: 10508–10521.

[40] Xu HJ, Dong HL, Liu XT, *et al.* High-temperature oxidized Mo_2CT_x MXene for a high-performance supercapacitor. *ACS Appl Mater Inter* 2023, **15**: 53549–53557.

[41] Surdu-Bob CC, Saied SO, Sullivan JL. An X-ray photoelectron spectroscopy study of the oxides of GaAs. *Appl Surf Sci* 2001, **183**: 126–136.

[42] Lykiema J, Sing KSW, Haber J, *et al.* Reporting physisorption data for gas/solid systems. *Pure & App Chem* 1984, **4**: 603–619.

[43] Zeng XJ, Jiang X, Ning Y, *et al.* Construction of dual heterogeneous interface between zigzag-like Mo–MXene nanofibers and small CoNi@NC nanoparticles for electromagnetic wave absorption. *J Adv Ceram* 2023, **12**: 1562–1576.

[44] Wang L, Lu JT, Zhang JL, *et al.* Facile preparation and high microwave absorption of flower-like carbon nanosheet aggregations embedded with ultrafine Mo_2C. *J Colloid Interf Sci* 2023, **641**: 729–736.

[45] Wen CY, Li X, Zhang RX, *et al.* High-density anisotropy magnetism enhanced microwave absorption performance in $Ti_3C_2T_x$ MXene@Ni microspheres. *ACS Nano* 2022, **16**: 1150–1159.

[46] Du H, Zhang QP, Zhao B, *et al.* Novel hierarchical structure of MoS_2/TiO_2/$Ti_3C_2T_x$ composites for dramatically enhanced electromagnetic absorbing properties. *J Adv Ceram* 2021, **10**: 1042–1051.

[47] Sun MX, Wang DR, Xiong ZM, *et al.* Multi-dimensional Ni@C–CoNi composites with strong magnetic interaction toward superior microwave absorption. *J Mater Sci Technol* 2022, **130**: 176–183.

[48] Huang WH, Zhang XX, Zhao YN, *et al.* Hollow N-doped carbon polyhedra embedded Co and Mo_2C nanoparticles for high-efficiency and wideband microwave absorption. *Carbon* 2020, **167**: 19–30.

[49] Qin M, Zhang LM, Wu HJ. Dielectric loss mechanism in electromagnetic wave absorbing materials. *Adv Sci* 2022, **9**: 2105553.

[50] Wang G, Li CF, Estevez D, *et al.* Boosting interfacial polarization through heterointerface engineering in MXene/graphene intercalated-based microspheres for electromagnetic wave absorption. *Nano-Micro Lett* 2023, **15**: 152.

[51] Wu CW, Zhang F, Zhi Q, *et al.* From binary to ternary and back to binary: Transition of electromagnetic wave shielding to absorption among MAB phase Ni_3ZnB_2 and corresponding binary borides $Ni_{n+1}B_n$ (n = 1, 3). *J Adv Ceram* 2023, **12**: 2101–2111.

[52] Meng XW, Qiao J, Yang YF, *et al.* Three-dimensional porous manganese oxide/nickel/carbon microspheres as high-performance electromagnetic wave absorbers with superb photothermal property. *J Colloid Interf Sci* 2023, **629**: 884–894.

[53] Qiao LJ, Bi JQ, Yang Y, *et al.* *In-situ* synthesis of multi-principal-element $(Mo_{0.25}Cr_{0.25}Ti_{0.25}V_{0.25})_3C_2T_x$ MXene-based composites with enhanced electromagnetic wave absorption. *Ceram Int* 2023, **49**: 40498–40510.

[54] Wang L, Cai ZX, Su L, *et al.* Bifunctional SiC/Si_3N_4 aerogel for highly efficient electromagnetic wave absorption and thermal insulation. *J Adv Ceram* 2023, **12**: 309–320.

[55] Liu PB, Zheng SY, He ZZ, *et al.* Optimizing integrated-loss capacities via asymmetric electronic environments for highly efficient electromagnetic wave absorption. *Small* 2024, **20**: 2403903.

[56] Shi YX, Liang BQ, Gao H, *et al.* Research progress on spherical carbon-based electromagnetic wave absorbing composites. *Carbon* 2024, **227**: 119244.

[57] Gou JL, Chang YK, Liu S, *et al.* Solid solution strategy modulated defects engineering of $(Cr_{1-x}V_x)_2AlC$ MAX phase toward superior electromagnetic wave absorption. *Rare Metals* 2024, **43**: 3205–3219.

[58] Liu PB, Gao S, Wang Y, *et al.* Metal-organic polymer coordination materials derived Co/N-doped porous carbon composites for frequency-selective microwave absorption. *Compos Part B Eng* 2020, **202**: 108406.

[59] Xu HL, Yin XW, Li XL, *et al.* Thermal stability and dielectric properties of 2D Ti_2C MXenes via annealing under a gas mixture of Ar and H_2 atmosphere. *Funct Compos Struct* 2019, **1**: 015002.

[60] Ning MQ, Lu MM, Li JB, *et al.* Two-dimensional nanosheets of MoS_2: A promising material with high dielectric properties and microwave absorption performance. *Nanoscale* 2015, **7**: 15734–15740.

[61] Jin ZY, Fang YF, Wang XX, *et al.* Ultra-efficient electromagnetic wave absorption with ethanol-thermally treated two-dimensional Nb_2CT_x nanosheets. *J Colloid Interf Sci* 2019, **537**: 306–315.

[62] Fan BB, Li N, Dai BZ, *et al.* Investigation of adjacent spacing dependent microwave absorption properties of lamellar structural $Ti_3C_2T_x$ MXenes. *Adv Powder Technol* 2020, **31**: 808–815.

[63] Zhu LL, Wu WW, Chen JJ, *et al.* High-performance electromagnetic wave absorption by two-dimensional mesoporous monolayer $Ti_3C_2T_x$ MXene. *Chem Eng J* 2024, **488**: 150649.